# SOLAR IRRADIANCE FORECASTING USING HEMISPHERICAL SKY IMAGES

## M.Alonso[a], P.Blanc, S.Travadel

a. Mines ParisTech, CRC (Center of Research on Risks and Crisis) research intern,
marius.alonso@mines-paristech.fr

**Key words :**  solar irradiance, estimation, forecasting, cloud segmentation, optical flow, differential geometry

**Abstract :**  This paper aims to improve the current state-of-the-art methods of solar irradiance prediction using hemispheric images, with particular attention to the geometry specific to these hemispheric images. The method used is based on the calculation of a local optical flow after projection, in order to overcome the deformations related to this geometry.

## 1   Introduction

Solar energy plays a key role in the energy transition we need to undertake to reduce the impact of climate change. Its potential is important, but it has the disadvantage of being based on solar illumination, which can show strong and rapid variations. It can for example double or drop by half in the space of 5 minutes. In our case study, an isolated gold mine in Mali, these variations in power supplied by the solar plant are compensated by diesel generators. The ignition of the latter takes 10 to 15 minutes. Thus, in order to control these two energy sources in the best possible way, the question of predicting the solar illumination at 15 minutes arises.

In the rest of the article, the prediction is to be made from hemispherical images of the sky, taken with a "fish-eye" camera every minute. This type of lens applies a strong distortion to the physical situation: the apparent movement of clouds on hemispheric images is not rectilinear.
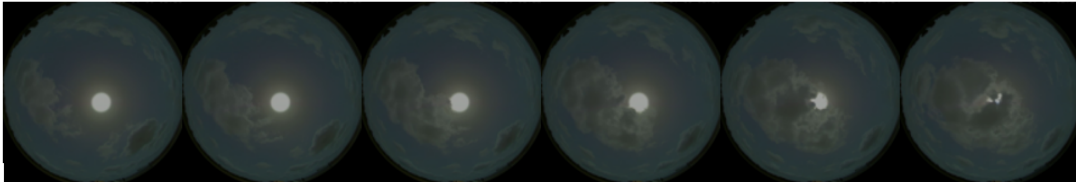


Figure 1: Succession of 6 hemispheric images taken every minute

Current state-of-the-art model developed by V. Le Guen [1] gives fairly good predictions of solar irradiance at 5 minutes, but does not seem to model cloud motion correctly. To train his model, V. Le Guen uses raw fish-eye images. Our hypothesis is that the neural network is not able to learn the particular geometry related to the fish-eye camera.

## 2   Metrics used

Here, we note $y(t_i)$ the value of the irradiance at time $t_i$, and $y^i$ the prediction or estimate of this value by the model. In the following sections, the estimation and prediction models are evaluated by (at least one of) the following metrics, commonly found in litterature :

- Normalized root mean squared error - $nRMSE = \frac{\sqrt{\frac{1}{N}\sum (y(t_i)-y^i)^2}}{\bar{y}}$

- Mean absolute error - $nMAE = \frac{1}{N}\sum |y(t_i) - y^i|$

The choice to convert RMSE to a relative error measure (nRMSE), unlike MAE, is arbitrary.

In addition, the results of the prediction models are compared with the persistence. This baseline consists in predicting the irradiance at time $t_{i+\Delta i}$ as the irradiance at time $t_i$ :

$$y_{persistence}^{i+\Delta i} = y(t_i)$$

# 3 Two approaches

## 3.1 An attempt to refine the model of V. Le Guen

First, experiments were carried out with the model of V. Le Guen, to try to verify our hypothesis. It was attempted to train the model with images of the sky having undergone different preprocessings:

- **Planar projection :** The base image is projected on a plane orthogonal to the zenith of the observer. The projection isn't complete : some parts of the original fish-eye image are lost. The plane is located at a certain altitude H from the position of the observer. In practice, the only parameter that matters in the calculations is the dimensionless ratio between the altitude of the projection plane and its extent. It is set at 0.2 for this section : for a layer of clouds located at an altitude of 4 km, we obtain a field of view of 20 km.

- **Crop :** The base image is cropped to reduce the amount of wasted information on the corners.

- **Sun-centered angular (SCA) :** The projection described by Q. Paletta [2] is here used. The x-axis of the projection describes the angular distance between the point to be projected and the center of projection, while the y-axis describes the angle between the direction from the center of projection to the point to be projected and a standard fixed direction (here $(0, -1)$).

Beside these preprocessings, the training was tested with RGB images, and (R-B)/(R+B) images, this operation contrasting in principle more the clouds [3] (More precisely, the channel (R-B)/(R+B) has the exact following formula: $\min(1, \max(0, 2.7\frac{R-B}{R+B} + 0.5)))$.



Figure 2: Illustration of various preprocessings : base image, (R-B)/(R+B), planar projection, SCA projection

The model was trained on a 9-day set of image data and associated irradiance, and evaluated on the 10th day. The results for a prediction at 5 minutes, in nRMSE, are the following :

| Image size | Channels | Projection | | | | Persistence |
|---|---|---|---|---|---|---|
| | | fish-eye | planar | cropped | SCA | |
| 64x64 | RGB | 0.21 | 0.21 | 0.22 | 0.20 | 0.28 |
| | (R-B)/(R+B) | 0.22 | 0.25 | 0.24 | 0.22 | |
| 128x128 | RGB | 0.22 | 0.24 | 0.24 | 0.22 | |

Table 1: Results of experimentation with V. Le Guen model

We found little to no improvement, both in the prediction of solar irradiance, and in the prediction of cloud displacement, while these preprocessings could have made the model tend to better understand the camera geometry.

## 3.2 A more classical approach

The results of the first approach suggest that an LSTM convolutional neural network is not able to correctly predict cloud motion, given the particular geometry of the problem.Thus, in the rest of the paper, the preferred approach is a more classical one, which divides the prediction of irradiance task into two distinct blocks:

- **Prediction of the future sky image**

- **Estimation of irradiance given the predicted sky image**

# 4 Method

## 4.1 Estimation of solar irradiance

### 4.1.1 The model : A convolutional neural network

The estimation is performed by a convolutional neural network, taking as input images projected in the zenithal plane, and reduced to 64x64 format. The CNN is made of the following layers :

| layer type | layer size | number of channels |
|---|---|---|
| Convolutional | 64x64 | 8 |
| Max pooling | 32x32 | 8 |
| Convolutional | 32x32 | 16 |
| Max pooling | 8x8 | 16 |
| Convolutional | 8x8 | 32 |
| Max pooling | 2x2 | 32 |
| Fully connected | 128 | 1 |
| Fully connected | 32 | 1 |
| Fully connected | 8 | 1 |

Table 2: Layers of the estimator

### 4.1.2 The baseline : A random forest regressor

To clarify the impact of the different estimation parameters, the CNN results are compared to those obtained by a random forest model, trained on three distinct observations:

- the altitude of the sun (i.e. the angle of the sun's direction with the surface, an angle of 90° meaning the sun is at the zenith)

- the number of visible solar pixels

- the average of the (R-B)/(R+B) channel over the whole image

### 4.1.3 Results

The training is performed on a set of 38 days (non-consecutive among 63 days) of image data and associated irradiance, minute by minute. The CNN model is trained on all weather conditions, and on images from 9:20 to 16:30, which corresponds roughly to a solar altitude higher than 37°. The images used for training are projected in the zenith plane (see 3.1), with an altitude/span ratio of 0.2. The evaluation of CNN model and baseline is performed on the remaining 25 days of data.

The results are the following :

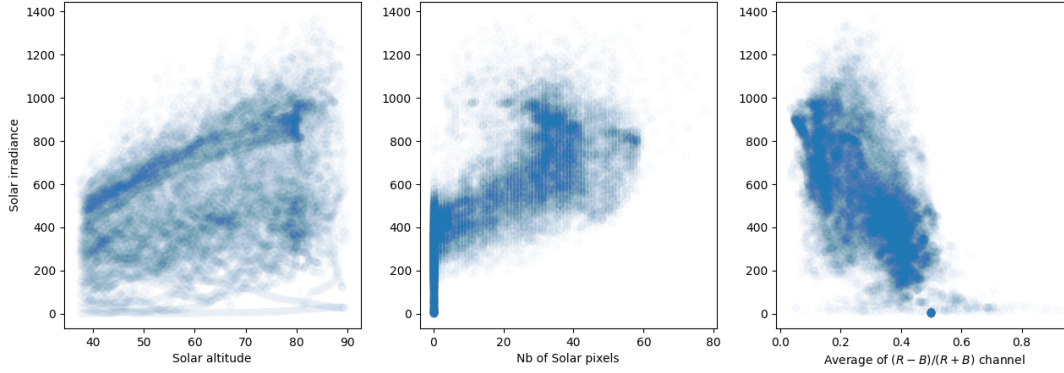| Model | CNN | Random forest |
|---|---|---|
| nRMSE | 0.18 | 0.24 |
| MAE in $W.m^{-2}$ | 68 | 100 |

Table 3: Results of the two estimators

Figure 3: Relationship between the different observations used by the baseline estimator and the irradiance
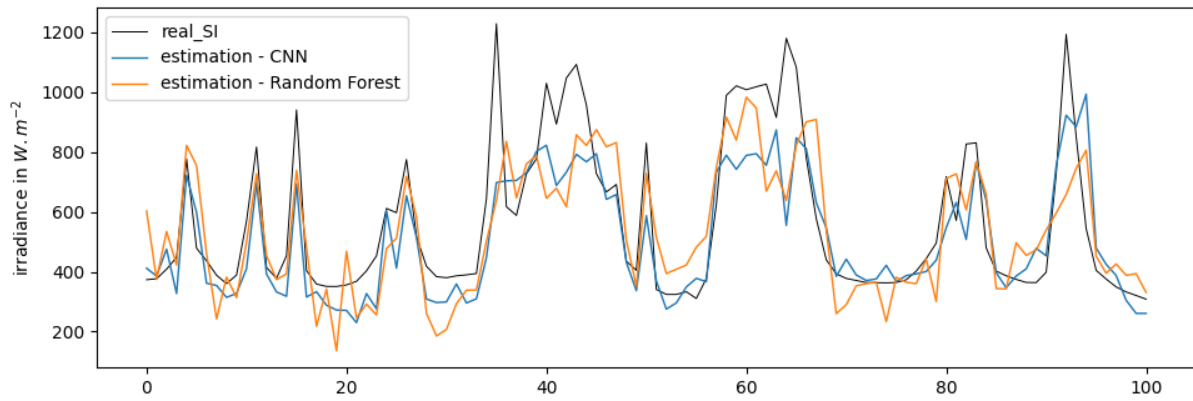


Figure 4: Example of an estimation over a 100-minute period on a cloudy day

Both models seem to follow correctly the variations of the irradiance signal. The CNN seems to be a little more accurate in its estimation of their amplitudes.

It is interesting to note that, among the observations used by the random forest, the one that is most important in its decision is the number of solar pixels. Its importance is quantified at 66%, against 21% for the solar altitude, and 13% for the (R-B)/(R+B) channel average. We also find this emphasis on the number of solar pixels in the CNN estimate, as illustrated by Figure 5. This finding reinforces our belief that it is necessary to build a local and accurate cloud propagation model, whose main objective is to determine whether a cloud is about to partially or totally obscure the sun in the next few minutes.

## 4.2 Prediction of future sky image by cloud propagation

### 4.2.1 Cloud segmentation

Cloud segmentation is mainly based on the (R-B)/(R+B) channel, traditionally used in the literature [3]. High values in this channel correspond to clouds, and low values to blue sky. The main difficulty of this technique is to remove from the segmentation the halo surrounding the sun, which does not follow the path of the clouds. This halo is particularly pronounced in the case of our study (a mine in Mali), as the local sky is often dusty and hazy.

In order to reduce the halo on the (R-B)/(R+B) images, the implemented coarse segmentation algorithm, greatly inspired by the work of Y. Tchouboukoff [4], performs a 2-means partitioning on angular sections of concentric rings centered on the sun. In practice, the algorithm works on about 50 concentric rings extending from the edge of the sun to the boundaries of the hemispheric image, each ring being divided into 8 angular sectors. On each angular section, the mean that seems most likely to correspond to the halo is subtracted

Once the (R-B)/(R+B) image has undergone the halo reduction process, it is segmented according to empirical thresholds defined beforehand (all pixels below 0.03 are marked as sky, and all pixels above 0.18 are marked as
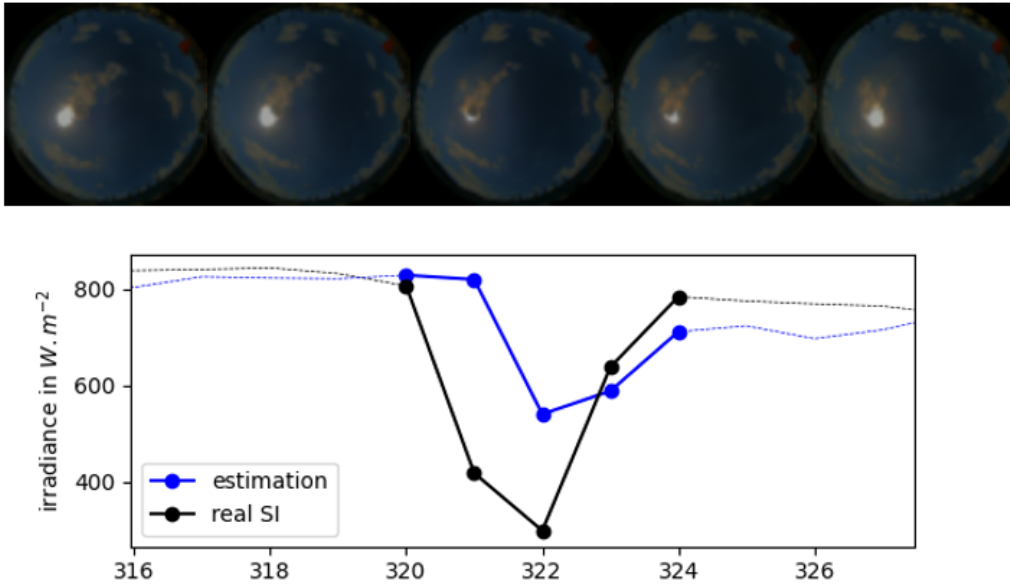
Figure 5: Delayed estimation of an irradiance drop. The CNN was misled by the number of visible solar pixels.
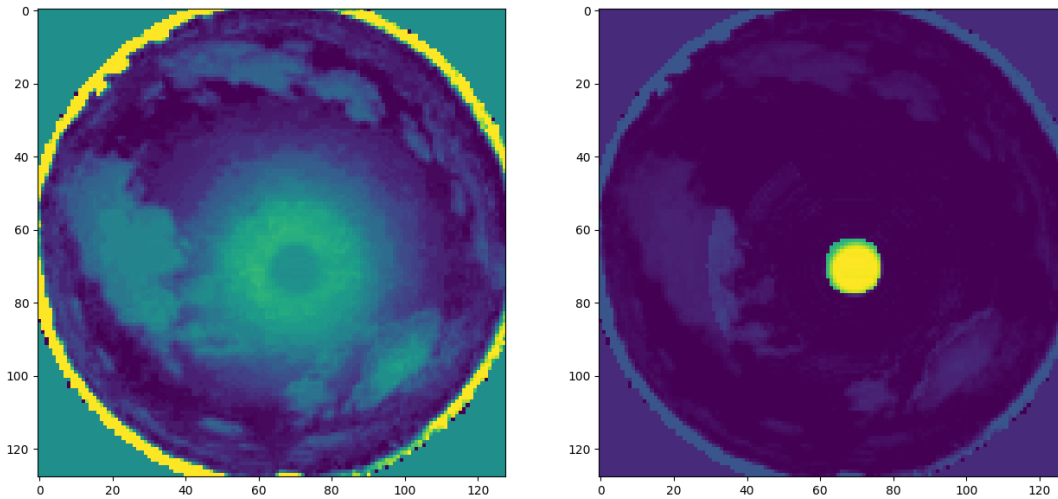


Figure 6: Halo reduction during segmentation in a basic case

cloud). The belonging of the rest of the pixels is determined by the watershed technique described in the paper by Y. Tchouboukoff [4].

This algorithm is not very satisfactory in practice (see 6.1.1), and also has the disadvantage of being relatively slow, taking 5 to 10 seconds per image.

### 4.2.2  Cloud Motion Vectors (CMV) computation

Once we have obtained the position of the clouds thanks to their segmentation, we need to calculate their speed. Here, the optical flow technique [5] is used on two successive images spaced one minute apart. As the displacements are large (sometimes more than ten pixels), a coarse-to-fine approach is adopted: a first approximation of the optical flow is computed iteratively on low resolution images, then refined on high resolution images.

The optical flow is calculated on the zenith projection of the fish-eye image described in part 3.1, in 512x512 format. This time, it is decided to take a height/extent ratio of 0.1. The channel used for the optical flow is the (R-B)/(R+B) channel, already used before.

To take into account the particular geometry of the camera and the inherent deformations that it generates, and for more accuracy in the propagation of clouds, it is calculated locally. The optical flow field is computed on

a grid of apodized windows (standard deviation of 42 pixels) of size 128x128, each spaced by 32 pixels. Thus, this makes a total of 169 calculation windows.



Figure 7: On the left, the computed optical flow field, and on the right, a calculation window

The dimensions of the computational windows were determined by the trade-off between high granularity of the cloud displacement field, and stability of the computation (ability to capture large displacements, blue sky disturbances).

### 4.2.3 Displacement of clouds

With their position and speed, we are now able to move the clouds. For simplicity, in this study, we consider that the CMV field is eulerian and stationary: it is not attached to the clouds but is fixed in the projection, and it does not vary during the forecast time. The propagation of the clouds is achieved by a simple translation of the computational windows of the optical flow, which intersect, ensuring continuity of the resulting image. The propagation is applied to the segmentation mask and to the segmented part of the RGB image. Finally, a clear sky model covers the background i.e. the non-segmented part.

## 5 Results

### 5.1 General comment

The results obtained, although promising, remain rather inconsistent. Because of the many problems that remain in the model, as detailed below, we were unable to obtain a quantitative assessment of our predictor. Nevertheless, the forecasting examples illustrated after show that the propagation/estimation forecasting technique can be successful. Moreover, the irregularity of the obtained CMV fields demonstrates the importance of the local computation of the optical flow and the consideration of the camera geometry.

### 5.2 Examples of prediction

In Figures 8 and 9, 4 successive outcomes of the model are highlighted, at t, t+5, t+10, t+15 and t+20, t being the instant chosen to start the forecast. For each of the 4 highlighted moments, we find on the left the sky actually observed, and on the right a prediction of the sky image by propagation. On the right images is superimposed the CMV field at time t. Below these zooms on the model operation, we find the minute-by-minute result of the model prediction (in blue), compared to the irradiance value estimated from the real sky image (in dotted blue), and to the irradiance actually observed (in orange).

#### 5.2.1 First example: a sudden drop in irradiance

On the first example (Figure 8), we see that the cloud coming from the left is propagated quite precisely, and thus obscures the sun in a rather simultaneous way between the real image and the propagated image. Note that the
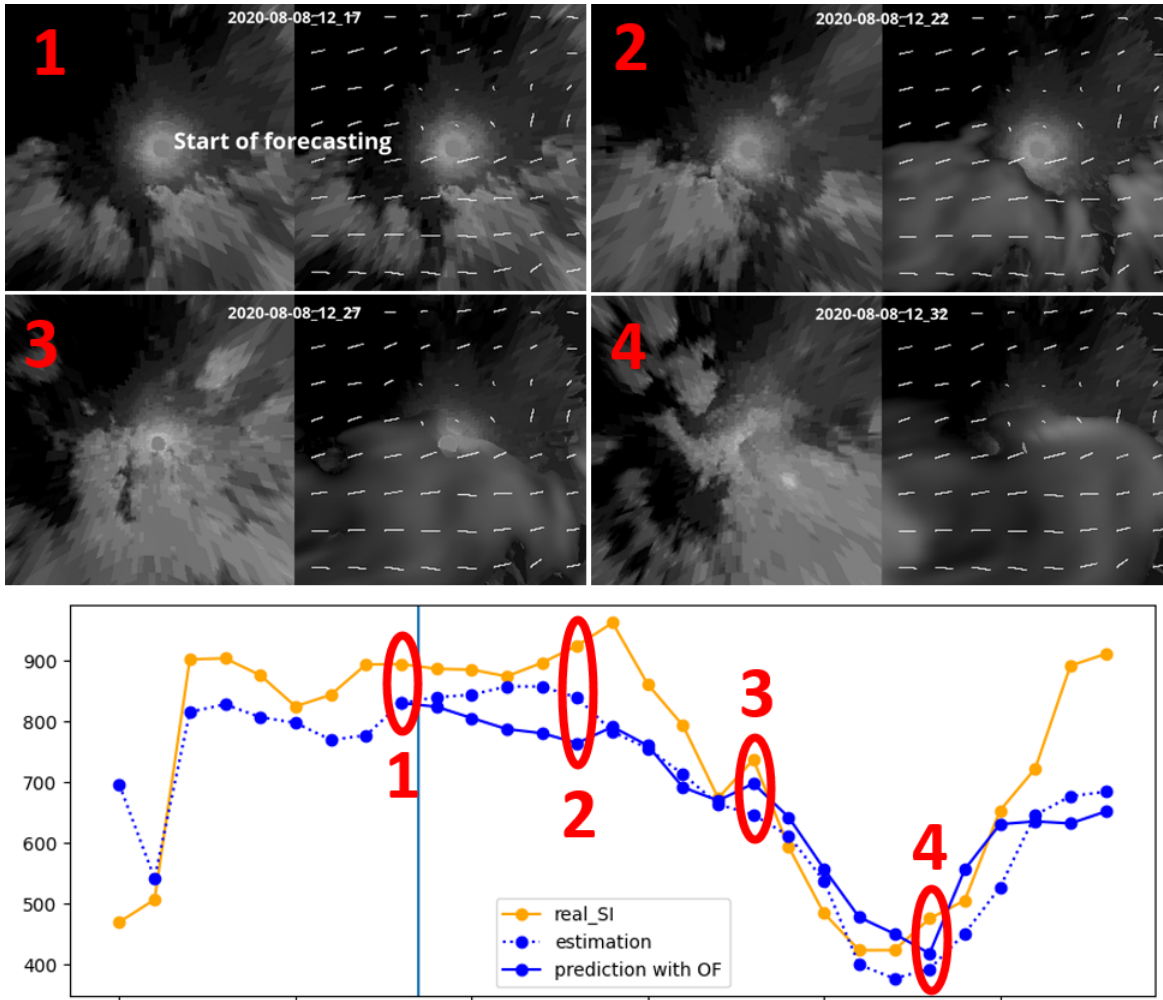
Figure 8: Successful prediction of an irradiance drop at 15 minutes

evolution of its color in the channel (R-B)/(R+B) can not be modeled by cloud propagation.

### 5.2.2 Second example: an irradiance that remains at a high level

On the second example (Figure 9), one can see that the displacement of the first cloud coming from the lower left corner is rather well modeled. This one, in reality as in the simulation, almost touches the sun, without obscuring it. The movements of the other clouds are also well modeled, except the second cloud coming from the lower right corner. In the model, it occupies after 15 minutes all the lower right corner and is about to obscure the sun and cause a fall of irradiance. In reality, it dissipates and the irradiance is not impacted for at least 20 minutes.

This example also reveals a certain bias of the model to predict regular decreases in irradiance, even without solar obscuration. The range of irradiance generally observed when the sun is visible is between 600 and 900 $W.m^{-2}$. Here, the estimator favors the lower values of this range, without however going outside of it. This is therefore not a problem in absolute terms (no drop in irradiance is wrongly predicted), even if the bias should be corrected.
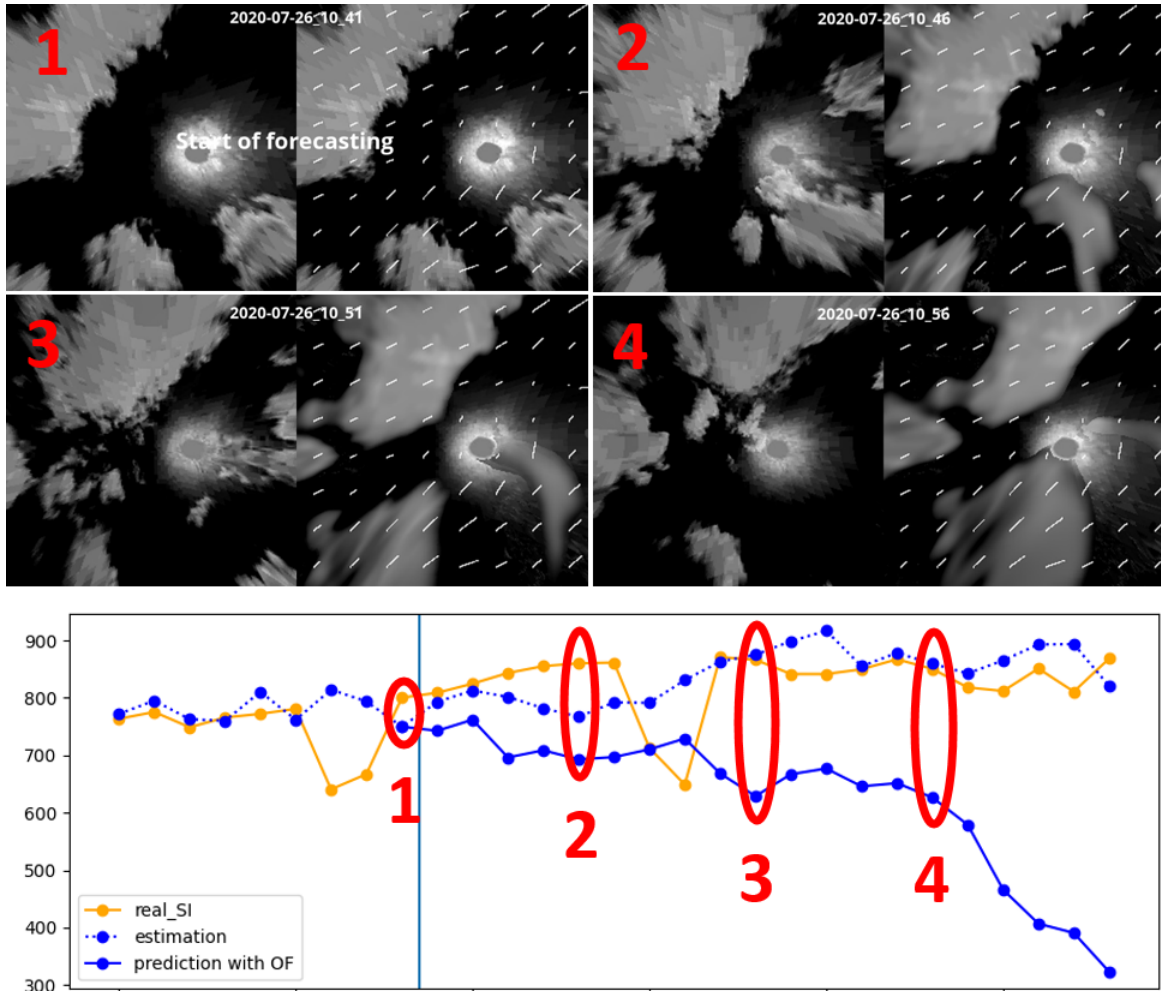
Figure 9: Relatively successful prediction of no irradiance drop at 15 minutes

# 6 Perspectives and limitations

## 6.1 Perspectives

### 6.1.1 Segmentation issues

The implemented segmentation algorithm can easily be defeated. When a cloud is close to the sun, as depicted in Figure 10, it is often very badly segmented. Indeed, the segmentation task is extremely delicate, the color of the halo surrounding the sun and that of the cloud being almost identical. Moreover, when the sun is just piercing an overcast sky (the clouds are not opaque enough to mask it), the segmentation algorithm erroneously considers that the clouds surrounding the sun correspond to its halo. The only way to improve the segmentation process in these problematic cases is to consider the image metrics i.e. the pixel layout, and not their simple color.

In a second step, it would be desirable to perform a multi-layer segmentation. Indeed, in many cases, a lower layer and an upper layer of clouds are identifiable, neither advancing at the same speed, nor in the same direction. Their evolution, although predictable, cannot be modeled with a single layer model.

### 6.1.2 Parallax issues

The data available to us for this study included several solar irradiance sensors, all located on the same mining facility, a few hundred meters apart. None of the sensors were located at the exact location of the camera. In addition, the estimator results were highly dependent on the sensor chosen, ranging from 0.18 to 0.25 in nRMSE. We opted for the sensor with the best correlation with the number of solar pixels visible in the hemispherical camera images. It is also the one giving the best results in estimation.
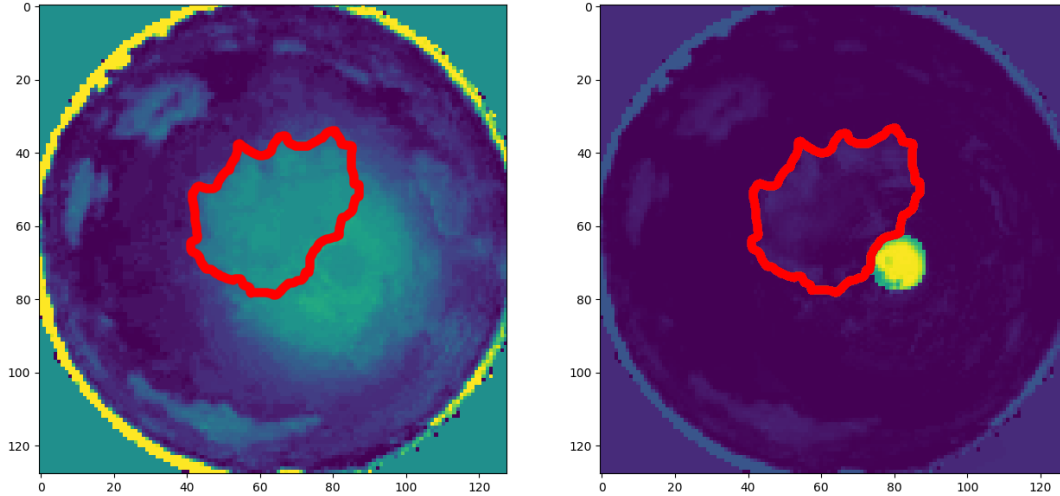
Figure 10: On the left, image of the sky in (R-B)/(R+B) where a large cloud touches the sun. On the right, same image after reduction of the halo by the segmentation algorithm. The probable outlines of the cloud are marked in red.
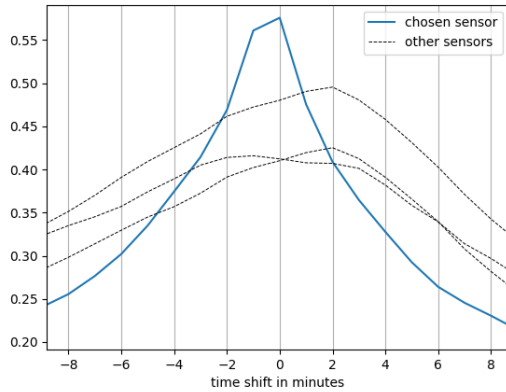


Figure 11: Average correlation over 31 days between the amount of solar pixels on the sky image and 4 different irradiance signals
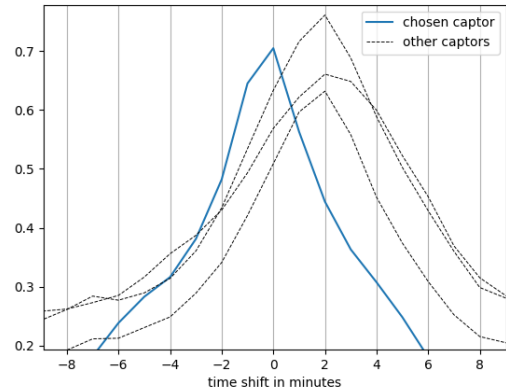


Figure 12: Example of a day for which a higher correlation is reached with another sensor, tainted by a time lag

Considering the example in Figure 12, it is likely that improvements in the estimation of solar irradiance are possible provided that the camera and the irradiance sensor are positioned close enough to each other.

## 6.2 Limitations of classical approach

By favouring the classical approach to the one proposed by V. Le Guen, some atmospheric phenomena influencing irradiance can no longer, to a certain extent, be modelled and taken into account. Among these different phenomena, we can mention two that have a considerable impact on solar irradiance:

- **The diversity and variability of the "clear sky":** it can be more or less hazy or dusty, without clouds clearly standing out, and it can change within a few minutes.

- **The advection phenomena:** clouds can appear or disappear in the space of a few minutes

In a substantial number of situations, propagating the clouds does not seem to be sufficient. It would then be potentially useful to combine the classical approach with the "deep learning" approach. Future works can consider a CNN-LSTM network correcting a first sky image given by cloud propagation.
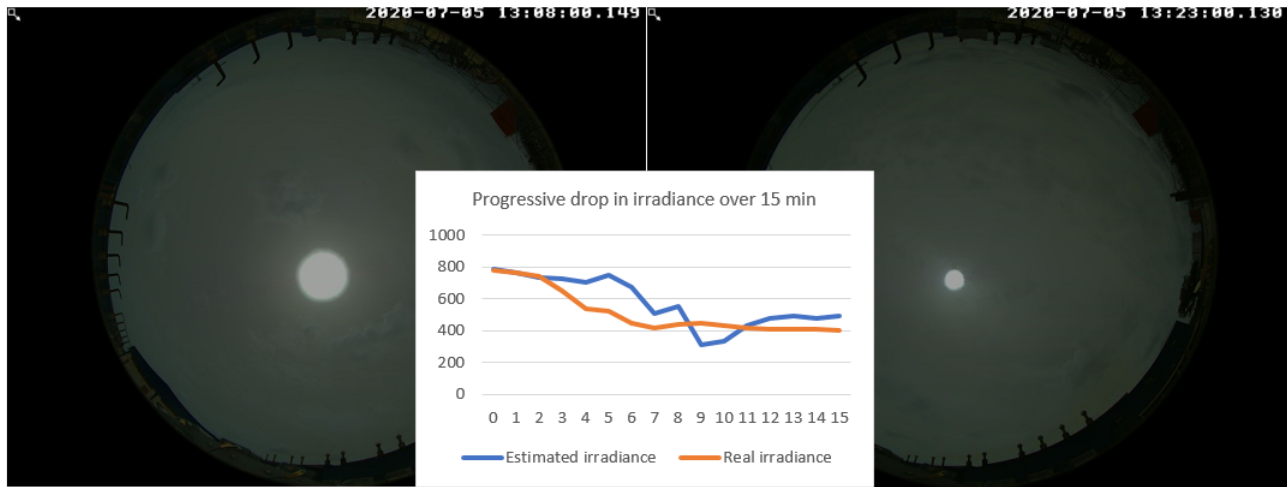
Figure 13: Situation where the "clear sky" is particularly hazy, and where a progressive drop in irradiance of 50% in less than 15 min is observed

# Acknowledgements

# References

[1] V. Le Guen, N. Thome, A Deep Physical Model for Solar Irradiance Forecasting with Fisheye Images, 2020

[2] Q. Paletta., A. Hu, G. Arbod, P. Blanc, J. Lasenby, SPIN: Simplifying Polar Invariance for Neural networks Application to vision-based irradiance forecasting, 2021

[3] M. Hasenbalg, P. Kuhn, S. Wilbert, B. Nouri, A. Kazantzidis, Benchmarking of Six Cloud Segmentation Algorithms for Ground-Based All-Sky Imagers, 2020

[4] Y. Tchouboukoff, P. Blanc, S. Travadel, Physically Constrained Neural Network for Cloud Coverage Nowcasting, 2021

[5] B. D. Lucas, T. Kanade, An iterative image registration technique with an application to stereo vision, 1981